Nuclear Engineering and Technology 55 (2023) 3754–3767

Contents lists available at ScienceDirect

Nuclear Engineering and Technology

journal homepage: www.elsevier.com/locate/net

Original Article

Numerical simulation of air discharged in subcooled water pool

Y. Córdova [a, *], D. Blanco [a], Y. Rivera [a], C. Berna [a, b], J.L. Muñoz-Cobo [a], A. Escrivá [a]

[a] Instituto Universitario de Ingeniería Energética, Universitat Politècnica de València (UPV), Camino de Vera 14, 46022, Valencia, Spain
[b] Departamento de Estadística, Investigación Operativa Aplicadas y Calidad, Universitat Politècnica de València (UPV), Camino de Vera 14, 46022, Valencia, Spain

ARTICLE INFO

Article history:
Received 31 March 2023
Received in revised form
8 June 2023
Accepted 25 June 2023
Available online 26 June 2023

Keywords:
Multiphase flow
Suppression pool
Computational fluid dynamic
Non-condensable gas
Jet
Air discharge

ABSTRACT

Turbulent jet discharges in subcooled water pools are essential for safety systems in nuclear power plants, specifically in the pressure suppression pool of boiling water reactors and In-containment Refueling Water Storage Tank of advanced pressurized water reactors. The gas and liquid flow in these systems is investigated using multiphase flow analysis. This field has been extensively examined using a combination of experiments, theoretical models, and Computational Fluid Dynamics (CFD) simulations. ANSYS CFX offers two approaches to model multiphase flow behavior. The non-homogeneous Eulerian-Eulerian Model has been used in this work; it computes global information and is more convenient to study interpenetrated fluids. This study utilized the Large Eddy Simulation Model as the turbulence model, as it is better suited for non-stationary and buoyant flows. The CFD results of this study were validated with experimental data and theoretical results previously obtained. The figures of merit dimensionless penetration length and the dimensionless buoyancy length show good agreement with the experimental measurements. Correlations for these variables were obtained as a function of dimensionless numbers to give generality using only initial boundary conditions. CFD numerical model developed in this research has the capability to simulate the behavior of non-condensable gases discharged in water.

1. Introduction

The behavior of turbulent jets discharged in pools of subcooled water is of great interest for many industrial applications. These discharges can be of pure steam, pure non-condensable gases (NC) or mixtures of non-condensable gases and steam. Nozzles, spargers and injectors are commonly used as means of discharge. In the nuclear industry, the behavior of these jets plays a crucial role in the design of the safety systems incorporated into nuclear power plants. Several types of Light Water Reactors use the Direct Contact Condensation (DCC) mechanism by discharging the steam and NC gases into large pools of subcooled water. In this way, the subcooled pool absorbs the enthalpy excess liberated from the primary system, contributing to their depressurization. The main objective of DCC is to prevent containment pressurization and to enable primary system depressurization to allow the safety injection systems to act. This is a crucial part of the reactor safety design with the ultimate goal of preventing the release of radioactive fission products to the environment [1,2].

The Pressure Suppression Pool (PSP) of Boiling Water Reactors (BWR) has a dual function. During normal operation, it condenses steam injected through the multi-hole injection of the automatic depressurization system (ADS) or through large diameter blowdown pipes during Loss Of Coolant Accidents (LOCAs) [3]. Additionally, if the PSP is unable to perform its function, the lower containment volume may result in its rapid pressurization and, ultimately, its failure or venting to the atmosphere. Furthermore, PSP acts as a source of water for the Emergency Core Cooling System (ECCS), containment spray, and as a scrubber to clean up radioactive aerosols in the event of a core damage accident [4].

The In-Containment Refueling Water Storage Tank (IRWST) of Advanced Pressurized Water Reactors (APWRs) of Westinghouse performs similar functions as the PSP in the BWRs [5]. Upon activation of the Pilot-Operated Safety Relief Valve (POSRV), the water, air, and steam in the Safety Depressurization/Vent System (SDVS) discharge line are released sequentially into the IRWST [6]. The pool design must consider the thermohydraulic behavior of these

* Corresponding author.
E-mail addresses: yaicorc1@upvnet.upv.es (Y. Córdova), dablade@upv.es (D. Blanco), yaridu@upv.es (Y. Rivera), ceberes@iie.upv.es (C. Berna), jlcobos@iqn.upv.es (J.L. Muñoz-Cobo), aescriva@iqn.upv.es (A. Escrivá).

https://doi.org/10.1016/j.net.2023.06.041

discharges (i.e., penetration and buoyancy lengths of the jet, existence of stratification, etc.).

In fluid mechanics, the flow of more than one fluid phase in a system is known as multiphase flow. In the case of a gas discharge in water, the type of multiphase flow is gas-liquid flow. Engineers and scientists use different approaches to study multiphase flow, including experiments, and analytical and computational tools. In recent years, the Computational Fluid Dynamics technique (CFD), validated by available experimental data, has also been used to simulate the multiphase flow and heat transfer characteristics produced when discharging steam/NC jets in subcooled water pools. Numerous researchers have extensively addressed this area of research through experiments, theoretical models and CFD simulations, which has expanded the existing databases [7].

In the experimental part, horizontal, vertical, and even inclined gas jet discharges have been investigated. Within the horizontal jets there are pure jets (non-buoyant jets) and buoyant jets. When dealing with pure non-buoyant jets, the density of the jet fluid and the surrounding ambient fluid become quite similar once the jet fluid has condensed. As a result, only the momentum force would be present. Buoyant jets occur when a low-density fluid is discharged at high velocity (significant momentum) through an orifice into a higher-density fluid. Initially, the momentum force (jet) dominates, but as it loses kinetic energy due to friction with the surrounding liquid and momentum transfer by condensation, the buoyancy force (plume) will dominate [8,9].

Upon leaving the nozzle, several regions can be distinguished in the buoyant jets. These regions include a jet-like region, a transition region from jet to plume, a plume-like region, a two-phase turbulent zone of gas dispersed in the liquid (dispersion zone), and a liquid recirculation zone (recirculating zone) [8]. Additionally, sloshing waves are formed at the free surface when the gas flow rate is sufficiently high [10,11]. The jet region is dominated by the remaining initial momentum, where the jet behaves as a continuum and does not disintegrate into rising bubbles until it moves far away from the nozzle. The transition region is characterized by a flow in which momentum and buoyancy forces are present with a similar contribution. Finally, there is the plume region, where mainly the buoyancy force dominates, and the bubbles break up and follow the direction dictated by buoyancy effects [8].

To characterize the behavior of the air jets, the characteristic lengths or measurements that define the jet geometry are used. Among the most studied parameters are the jet penetration length (the maximum distance the jet reaches measured from the center of the nozzle), the buoyancy length (distance from the end of the penetration length to the maximum penetration point of the jet) and expansion angle (angle measured from nozzle exit to the jet centerline to maximum width). These parameters depend on the characteristics of the nozzle, the fluid discharged and the pool. Numerous experimental techniques have been employed to determine these variables. These techniques range from intrusive methods like electro-resistive or optical probes submerged in water [12,13] to non-intrusive methods such as direct visualization using Charge-Coupled Device (CCD) cameras and (solid-state) illumination systems [8,14–16]. As the technologies available to researchers have improved, analyses have become more detailed and measurement methods have improved in accuracy. Data from experimental investigations have allowed the validation of models and empirical parameters in integral models.

Many researchers have used the direct visualization technique to determine these parameters in their experiments. They have developed correlations to define them empirically, usually based on a modified Froude number or a modified jet force number (function of the pressure ahead of the nozzle and nozzle throat diameter) [8,17–20]. This technique has also been used to study the penetration length and condensation oscillation of steam jets immersed in subcooled water, obtaining correlations that allow calculating this length dimensionless [21–25].

One of the main results obtained so far is that the difference between the densities of the discharged fluid and the medium facilitates the jet to be less stable [26]. In addition, Hoefele and Brimacombe [18] showed that the penetration distance and flow regimes were strongly related to the Froude number and the ratio of fluid densities. While Engh and Nilmani [27] indicated that viscosity could retard the gas flow velocity. The results of Dai et al. [28] show that high-velocity jets discharged in stagnant water can induce pressure pulsations at the nozzle outlet. In turn, Shi et al. [29] posit that these supersonic air jets can cause large flow oscillations, which may be strongly linked to shock waves manifested in the gas phase. Several studies have indicated that in the air jet, the transition from the bubbling to the jet regime occurs at a critical Weber number of 2, regardless of the nozzle diameter [30].

Multiphase flow simulations using CFD codes remains as a challenging task due to the complex physics involved. The CFD code ANSYS CFX is a software tool mainly used by engineers, faculties, and researchers to understand and predict the behavior of fluids in various applications. It utilizes computational fluid dynamics (CFD) techniques to simulate fluid flow, turbulence, and heat transfer through a system or device. This software is often used in aerospace, automotive, and chemical engineering industries to design and improve products, processes, and systems, reduce development costs, and increase product reliability and safety [31,32].

ANSYS CFX has various features and capabilities for analyzing fluid flow problems. This software can be used to study a wide range of issues involving the flow of gases and/or liquids, heat transfer, and fluid-structure interactions. It offers a range of advanced turbulence models and heat transfer capabilities. It also includes post-processing and visualization tools to help the users to interpret and analyze the simulation results. ANSYS CFX includes a variety of multiphase models to simulate multiple fluid flows, bubbles, droplets, solid particles, and free surface flows. Two approaches, Eulerian-Eulerian Model and Lagrangian Particle Tracking are available for multiphase flow modelling in CFX. When the interest is focused on determining the trajectories of particles, droplets, and bubbles, it is advisable to use Lagrangian Particle Tracking, which performs the calculations by tracking particles. On the other hand, when the focus of the simulation is obtaining global information instead of the individual behavior of particles, droplets, or bubbles, it is preferable to use the Eulerian-Eulerian Model, which interprets the phase volume fractions as continuous functions of space and time [31,32].

The Eulerian-Eulerian Model employs two techniques: the interpenetrated continuum method and the weighted phase averaging. In the interpenetrated continuum method, the phases share the same volume and penetrate each other in space. In contrast, in the weighted phase averaging, the amount of the dispersed phase contained in each cell is quantified as a function of its volume fraction, and the interface structure is not available after averaging. Most multiphase flows are calculated as interpenetrated fluids in which the flow fields must be predicted for all fluids in the entire flow region [31].

The homogeneous turbulence equations for solving multiphase flows are the same as those for single-phase flows, except that the density and viscosity of the mixture are used. First, additional equations are included for the volume fraction of each fluid, i.e., the volume fraction occupied by that fluid when considered an interpenetrated continuum. Second, other terms are included in the transport equations for each phase to model interphase transfers, such as entrainment, heat, and mass transfer [31].

The usual approach when simulating turbulent flows is to use

the Reynolds Averaged Navier-Stokes equations (RANS). Within these, the most commonly used is the k-epsilon because this is a two-equation model that offers a good compromise between numerical effort and computational accuracy. Therefore, many researchers have used the k-epsilon model to solve their computational models [33–39]. Another appropriate approach is Large Eddy Simulation (LES) model, as shown by Li et al. [40]. Within this model, the time-dependent equations are solved for turbulent motion assuming that the eddies of a length scale smaller than a given size are not resolved and their effect is modelled by their average behavior. This approach is equivalent to filtering the Navier-Stokes equations according to the spatial discretization of the simulation. Although calculations using the LES turbulence model require higher computational cost, its results are much more accurate for unsteady and buoyant flows with large unsteady regions. A work comparing both models (k-e and LES) with experimental results using Particle Image Velocimetry (PIV) was developed by Dahikar et al. [41]. It showed a better agreement between the LES model and the experiments.

Due to the high complexity of the phenomena present in these floating jets, experimental studies and numerical simulations are still necessary to understand the behavior of gas jets discharged in subcooled water. This research presents the numerical validation of the experimental study performed by Harby et al. [8,9]. A deep comparison has been done for air discharges through different nozzle sizes and air mass flow rates in an aqueous medium. ANSYS CFX code has been employed for the simulations following the Eulerian-Eulerian multiphase flow approach.

In order to carry out the mentioned objectives, the study has been organized as follows: in section 2, a brief description of the experimental research previously carried out by other researchers and which will be the one to validate the computational model developed in this work will be made; the methodology used to perform the numerical model using ANSYS CFX is analyzed in section 3; the spatial discretization and the independence of the mesh results have been described in section 4; the main results of the simulations performed are presented in section 5; section 6 shows the validation of the developed computational model with experimental and theoretical results. While section 7 is devoted to exposing the main conclusions and their discussion.

2. Reference experimental study

The results presented in this paper were validated through experiments conducted at the Thermal-Hydraulic and Nuclear Engineering Research Laboratory of the Institute for Energy Engineering at the Polytechnic University of Valencia in Spain. These experiments were performed as part of a doctoral thesis, and the findings were subsequently published in two separate articles [8,9].

Fig. 1 shows the flow diagram of the experimental facility. It consists of an air compressed circuit linked to a rectangular stainless steel water tank (1000 x 400 × 750 mm). The sidewalls of the tank are transparent to enable flow visualization and optical measurements. To ensure a stable gas pressure and storage during experiments, a 0.1 m^3 gas tank was placed before the water pool. Additionally, the discharge was carried out horizontally using four straight stainless-steel tubes (nozzles) with inside diameters of 2, 3, 4, and 5 mm at a submergence depth of 200 mm above the tank bottom [9].

To maintain a constant mass flow rate to the nozzle, the pressure regulator valve was used in conjunction with the gas tank. A perforated flat plate was placed over the free surface of the water tank to regulate hydrodynamic pressure and to minimize surface waves. To examine the jet parameters, including penetration length and the interface between the jet and water ambient, a high-speed camera (CCD) and an illumination system were utilized. The Nikon AF Nikkor 50 mm f 1.8d lens-equipped CCD camera was used to capture shadowgraph images illuminated by six 500 W halogen lamps of a white-light lamp bank. The camera, computer, and illumination system formed the basis of the flow visualization technique [8,9].

Two flow rotameters from Key Instruments (series FR 4500), operating in parallel, were utilized to measure the mass flow rate. These rotameters had ranges of 4–50 l/min and 30–300 l/min. The pressures and temperatures were registered using Druck 1400-PTX pressure transducers (accurate to ±0.15%) and K-type thermocouples (accurate to ±0.1 °C), respectively. To minimize errors, different transducers and thermocouples were utilized to measure multiple temperature and pressure ranges. A National Instruments data acquisition system (model 6259 16-bit) and LABVIEW software were employed to monitor and control the different readings collected from the thermocouples and pressure transducers [9].

In order to obtain the parameters of the jet in the momentum region, 15,600 images were recorded at a 1.2 kHz sampling rate over a 13 s period for each experiment. For the buoyant region analysis, 9000 images were recorded at a 1 kHz sampling rate over a 9s period for each experiment. Under different initial conditions, the digital images were collected, saved, and examined to extract the interface position to measure the two-dimensional jet trajectories. A MATLAB script was used for image post-processing in a stepwise manner to obtain the perimeter of the jet and to measure the lengths by counting pixels numbers [9].

3. Numerical modelling with ANSYS CFX

3.1. Numerical model development

A three-dimensional two-phase model has been developed using the finite volume formulation. The geometry of the model consists of a rectangular tank with dimensions 1000 x 400 × 600 mm. The water level was considered at 500 mm, which would be the free surface between the water and the ambient air. The nozzle was located on one side of the tank, which would be the air inlet condition in the domain.

The Eulerian-Eulerian approach has been chosen using the method of interpenetrating continua. Both water and air have been simulated as continuum fluids, defining air as an ideal gas. Gravity effects have been considered, and the buoyancy model chosen is the Density Difference for both fluids. The multiphase model was considered non-homogeneous, and the Free Surface Model was considered to observe the free surface behavior between water and air at the exit of the pool. As there is no heat transfer, the Isothermal option at ambient temperature was used. For the turbulence approach, the homogeneous LES Dynamic model was used. The governing equations for this model are described below (Section 3.2-3.5).

3.2. Non-homogeneous multiphase model

A non-homogeneous multiphase model is a mathematical model used to describe the flow of multiple phases in a system. In inhomogeneous multiphase flows, the velocity fields are resolved separately, whereas all fluids share the pressure field. The fluids interact via interphase transfer terms. A system of partial differential equations (PDEs) describes the conservation of mass, momentum, and energy in a non-homogeneous multiphase model, which characterizes the flow of the distinct phases. These PDEs may be solved using numerical techniques, such as the Finite Element Method (FEM) or Finite Volume Method (FVM). In non-homogeneous models, the interphase transfer of momentum,

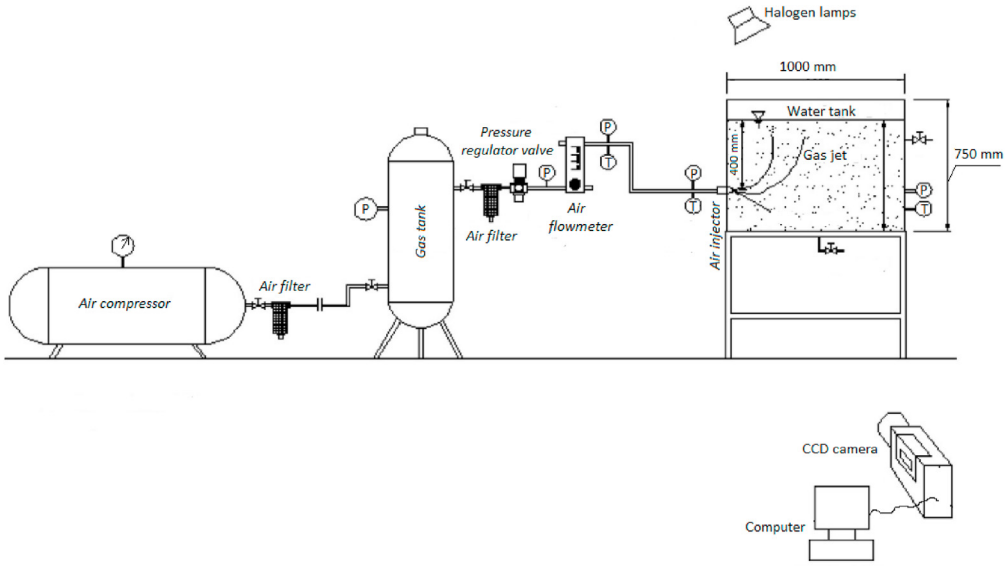

Fig. 1. Schematic diagram of the experimental facility for discharge jets in stagnant water based on experiments of Harby et al. [8].

energy and mass depends directly on the contact surface area between the two phases, i.e., the interfacial area per unit volume between phase α and phase β, known as the interfacial area density ($A_{\alpha\beta}$). The interfacial area density will be calculated depending on the chosen multiphase model. The Mixture Model was selected in this case since it is a straightforward model that treats both phases symmetrically. Therefore $A_{\alpha\beta}$ is calculated by Equation (1) [31]:

$$A_{\alpha\beta} = \frac{r_\alpha r_\beta}{d_{\alpha\beta}} \tag{1}$$

Where r_α and r_β are the volume fractions for the α and β phases, respectively. The interfacial length scale is denoted as $d_{\alpha\beta}$, is defined as the distance between two phases at the interface. This parameter can be determined by considering factors such as flow close to walls and turbulence models [31]. A value of $d_{\alpha\beta} = 1\ mm$ was used in this work, as it provides a suitable representation of the small-size entrained air bubbles observed in experimental research studies, such as the reference papers by Harby et al. [8,9]. Nevertheless, it is important to acknowledge that this variable is not directly indicative of bubble size, as the Mixture Model does not incorporate bubble size as an input parameter. Instead, the gas phase is considered by incorporating relevant physical properties through the void fraction.

A key advantage of using a non-homogeneous multiphase model is its ability to simulate complex multiphase flow systems, incorporating variations in the properties of the different phases within the system. However, no-homogeneous models can be more computationally intensive than homogeneous models, assuming that the properties of the different phases are constant throughout the system.

3.3. Momentum equation

The momentum equations are solved for each phase independently as a function of the volume fraction. The volume fraction r_α weights the multiphase momentum equation and contains two additional terms. Equation (2) shows the multiphase momentum equation for N_p phases for phase α.

$$\frac{\partial}{\partial t}(\rho_\alpha r_\alpha \boldsymbol{U}_\alpha) + \nabla \bullet (\rho_\alpha r_\alpha \boldsymbol{U}_\alpha \otimes \boldsymbol{U}_\alpha) = -r_\alpha \nabla p_\alpha + \nabla \bullet \left(r_\alpha \mu_\alpha \left(\nabla \boldsymbol{U}_\alpha + [\nabla \boldsymbol{U}_\alpha]^T\right)\right) + \sum_{\beta=1}^{N_p} \left(\Gamma_{\alpha\beta}\boldsymbol{U}_\beta - \Gamma_{\beta\alpha}\boldsymbol{U}_\alpha\right) + \mathbf{S}_{M\alpha} + \mathbf{M}_\alpha \tag{2}$$

The term $(\Gamma_{\alpha\beta}\boldsymbol{U}_\beta - \Gamma_{\beta\alpha}\boldsymbol{U}_\alpha)$ represents the momentum transfer induced by interphase mass transfer terms $\Gamma_{\alpha\beta}$ and $\Gamma_{\beta\alpha}$. $\mathbf{M}_\alpha$ represents the total interfacial force acting on the α phase due to the presence of other phases. When there are only two phases (α and β), the interfacial forces are equal and opposite, so the net interfacial forces sum to zero. The total interfacial force can be due to several independent physical effects. The total interfacial force can be affected by several factors, including interphase drag force (D), lift force (D), lubrication force (LUB), virtual mass force (VM), turbulence dispersion force (TD) and solid pressure force (S). As previously mentioned, Mixture Model corresponds to the approach employed to calculate the interfacial terms. This model treats both phases symmetrically and requires both phases to be continuous. Fluid properties are calculated as volume-averaged mixtures. The term ${M_{\alpha\beta}}^D$ (equation (3)) represents the drag force per unit volume exerted by phase β on phase α.

$${M_{\alpha\beta}}^D = C_D \rho_{\alpha\beta} A_{\alpha\beta} |U_\beta - U_\alpha| (U_\beta - U_\alpha) \tag{3}$$

Being $A_{\alpha\beta}$ the interfacial area per unit volume described in section 3.2 and C_D the drag coefficient defined by its commonly used value of 0.44. Other forces for bubble behavior are not employed, given that the focus of this study does not revolve around bubble hydrodynamics or interfacial heat transfer. However, drag forces, which effectively capture the velocity gradient, have been taken into account as they assume a dominant role in establishing connections with macroscopic behavior and jet penetration.

3.4. Continuity equation

The mass continuity equation describes the mass flow

relationship of mass entering and leaving a control volume and its internal mass change. Equation (4) shows the continuity equation for the α phase for a multiphase flow with N_p phases.

$$\frac{\partial}{\partial t}(\rho_\alpha r_\alpha) + \nabla \bullet (\rho_\alpha r_\alpha \boldsymbol{U}_\alpha) = \mathbf{S}_{MS\alpha} + \sum_{\beta=1}^{N_p} \Gamma_{\alpha\beta} \tag{4}$$

The term $\mathbf{S}_{MS\alpha}$ describes the user-specified mass sources and the term $\Gamma_{\alpha\beta}$ represents the mass flux per unit volume from the β-phase to the α-phase; this term is only used if the mass transfer occurs between phases.

3.5. Turbulence equation

Turbulence is a complex, chaotic motion of fluids characterized by irregular fluctuations in velocity, pressure, and temperature. One common approach to understanding turbulence is to use the Navier-Stokes equations directly with small time steps ad small sizes of the grid in a way known as direct numerical simulation (DNS) that is very time consuming, so for most practical problems, this approach cannot be used. There are several ways to modify the Navier-Stokes equations to account for the effects of turbulence in a simpler way. One of the most widely use approaches is the Reynolds-Averaged Navier-Stokes (RANS) equations, which involve averaging the Navier-Stokes equations over time and space to smooth out the turbulence fluctuations. Other approaches to modeling turbulence include large-eddy simulation (LES), Direct Numerical Simulation (DNS), and Scale-Resolving Simulation (SRS). Each of these approaches has its own strengths and limitations, and researcher often use a combination of techniques to study different aspects of turbulent flows.

In this work, the LES Dynamic model developed by Germano et al. [42] and Lilly [43] was used to model turbulence. The Smagorinsky model's limitations are overcome by this dynamic model, which utilizes information from the resolved turbulent velocity field to evaluate subgrid-scale (SGS) model coefficients. The model coefficient is no longer a constant and is automatically adjusted based on the flow type. The model is based on an algebraic identity that relates the subgrid-scale stresses at two different filter widths. The smaller filter width is determined by the mesh size, while an explicit filtering procedure is necessary for the larger filter width. Since the filter operates on unstructured meshes, a volume-weighted average of variables from the centers of neighboring elements to the corresponding vertex is employed. Due to requiring explicit filtering it consumes more computational time than an algebraic model such as the WALE or Smagorinsky models.

The eddy viscosity is obtained using the coefficient C_d, which was extracted from the filtering procedure carried out by Lilly (1992) using a least square approach to minimize the error. Then, the SGS viscosity μ_{SGS} can be calculated using Equation (5) [31].

$$\mu_{SGS} = \overline{\rho} C_d \Delta^2 \left|\overline{S}_{ij}\right| \tag{5}$$

Where $\overline{\rho}$ is the mean density, Δ is the grid filter scale (proportional to the grid size), $\overline{S}_{ij} = \left(\frac{\partial \overline{u}_i}{\partial x_j} + \frac{\partial \overline{u}_j}{\partial x_i}\right)/2$ is the magnitude of large-scale strain-rate tensor, and $\overline{u}_i$ is the large-scale velocity.

3.6. Boundary conditions and initialization

The simulation was performed for different nozzle diameters, from 2 mm to 5 mm. Several mass flow rates were defined for each one of the nozzle diameters simulated. These mass flow rates were defined as an inlet condition with a volume fraction of 1 for air. An opening at 500 mm from the bottom was configured at 0 Pa relative pressure, where only air could enter. All other boundaries were defined as no slip wall.

For the initialization of the model a relative pressure depending on both height and axial direction was used. The nozzle zone was set with an air volume fraction equal to 1 and with the relative pressure depending on the case studied. In the tank zone two volume fractions and two pressures were defined, one for water and the other one for air above the free surface. Initially, the water inside the rectangular tank is considered to be at stagnant.

3.7. Solution method

To obtain accurate and reliable results, it is important to follow CFD best practices. The most general guidelines for CFD simulation are clearly define simulation objectives, mesh selection, verify mesh quality, conduct sensitivity tests, validate results, and report the mesh used. Before starting the simulations, the objectives and expected results were defined, so it was decided to develop a three-dimensional two-phase model with the finite volume formulation using the commercial software ANSYS CFX 2022 R1. As the mesh is one of the most important components of CFD simulation, a mesh was selected that had the appropriate density and captured the important characteristics of the flow. The geometric model was discretized using an unstructured tetrahedral mesh which in dependence on the model and mesh quality varied from 120,000–480,000 nodes. Also, it is important to verify mesh quality by checking orthogonality, aspect ratio, and skewness. To ensure mesh independence, it is important to conduct sensitivity test on the mesh. If the results do not significantly change with increasing mesh density the mesh can be considered independent (Section 4) [44].

Transients of 6 s were performed in order to stabilize the flow and the transient statistics were saved for the last 2 s of each simulation, which is the same time interval that was recorded during the experiments. The time step used for all simulations was $5 \bullet 10^{-4}\, s$ and these simulations were considered to have converged when the sum of the residuals was less than 10^{-4}. A High-Resolution Advection Scheme and a Seconder Order Backward Euler Transient Scheme were used, which is a dynamic model between upward first order and second order [31,32]. A computer with an Intel(R) Xeon(R) processor at 2.10 GHz processor speed, 16 cores and 64 GB of RAM was used to perform all the calculations. After performing the simulation, it is important to validate the results, i.e., compare the simulation results with experimental data to ensure that they are accurate and reliable (Section 6).

4. Spatial discretization and mesh independence

The geometry was meshed using Meshing 2022 R1 software using non-structural (tetrahedral) meshes. Before solving all calculations, a mesh independence study was developed. This study was performed with the nozzle diameter of 4 mm and mass flow rate of 0.0124 kg/s for three meshes: a coarse mesh, a medium mesh, and a fine mesh, being the total number of nodes for each 121932, 243681 and 463156 respectively. The details of each of these meshes are shown in Table 1.

The mesh density at the nozzle inlet is relatively large with respect to other regions of the domain. The mesh quality was determined using the parameters Skewness, Orthogonal Quality and Aspect Ratio taking into account the values defined in the ANSYS Meshing Manual. Skewness is one of the main measures of quality for a mesh, it determines how close to the ideal (equilateral or equiangular, value of 0) a face or a cell is, while a value of 1 (worse) indicates a completely degenerate cell. The Orthogonal Quality is the opposite that Skewness, the range is between 0 (worst) and 1 (best). Orthogonal Quality is the angular deviation

Table 1
Details of different meshes analyzed.

	Coarse	Medium	Fine
Total number of nodes	121932	243681	463156
Total number of elements	665114	1361403	2643056
Turbulence model	LES Dynamic	LES Dynamic	LES Dynamic
Average Orthogonal Quality	0.78	0.79	0.8
Average Aspect Ratio	1.8	1.8	1.8
Average Skewness	0.21	0.21	0.2
Time step	6 ms	6 ms	6 ms
Mesh Type	No-Structural	No-Structural	No-Structural
Calculation time	20h 40min	1d 20h 40min	3d 15h 15min

of the vector placed at the center of the cell face, with respect to the vector joining the neighboring cell nodes. Aspect Ratio is the relation of the longest edge to the shortest edge. The ideal value is 1, in ANSYS CFX the values are best below 10 for some solvers and the acceptable range would be around 100, even in some cases below 1000 [45].

As can be seen in Fig. 2, the three mesh types have the same trend, but in the case of the medium mesh and the fine mesh the most similar distributions are shown. The percentage error between the fine and medium mesh was 3%, while between the fine and coarse mesh was 13%.

Therefore, the medium mesh was selected as the final mesh to perform all simulations to decrease the computational time (Fig. 3). Using the medium mesh ensures that the results are not sensitive to the size or shape of the mesh, because the results of the CFD simulation are only as accurate as the mesh used to represent the fluid flow.

5. Results and discussion

In the following section the results of the simulation are presented. The aim of this study is to investigate the behavior of jet discharges into stagnant water. Table 2 shows the matrix of simulations performed for the four nozzle diameters (d_2, d_3, d_4, d_5, whose subscript refers to the inner size of each of the nozzle in mm) and different air mass flow rates. A total of 15 simulations were carried out, not counting those performed for the mesh independence. The figure of merit that will allow to analyze the behavior of jet discharges is the air volumetric fraction, which will provide the zones where the air is located.

The Froude number is the ratio between the inertial and buoyancy forces of the jet. When the Froude number increases, the initial jet momentum becomes more dominant, and when the Froude number is small, the jet quickly becomes a plume. The Froude number is one of the primary dimensionless parameters that governs the flow. Some authors define the Froude number for a jet using Equation (6) and this same definition was used to calculate the Froude number in this work.

$$Fr_0 = \frac{u_0}{\sqrt{g(\Delta\rho/\rho_g)d_N}} \tag{6}$$

Where u_0 is the initial jet velocity at the nozzle exit, g is the gravity acceleration, $\Delta\rho/\rho_g$ is the ratio between the difference of densities (liquid and gas) and the gas density, and d_N is the nozzle diameter.

In addition to the Froude number, other important dimensionless numbers are the Reynolds number and Mach number. The Reynolds number is a measure of the relation of inertia forces to viscous forces in a fluid, Equation (7) shows this relationship. It is used to characterize fluid flow in different situations and to determine whether the flow is laminar or turbulent. The Mach number is a dimensionless measure of the jet velocity relative to the speed of sound in the medium, defined by Equation (8).

$$Re = \frac{\rho_g u_0 d_N}{\mu_g} \tag{7}$$

$$Mach = \frac{u_0}{u_s} \tag{8}$$

where μ_g is the gas dynamic viscosity and $u_s = \sqrt{\frac{\gamma RT}{M}}$ is the speed of sound in the medium.

5.1. Jet air behavior

When pure air is discharged into subcooled water, the jet motion is mainly influenced by two forces. Inertia forces, due to the velocity and properties of the air at discharge conditions, and buoyancy forces, mainly related to the difference in densities between the jet air and the pool water. The inertia forces become smaller as the jet develops (as the air moves away from the nozzle) and the buoyancy forces remain constant producing an upward momentum per unit volume $\int \Delta\rho\, g\, dt$. Initially the inertial forces are much larger than the buoyancy forces. This causes that in the initial discharge zone the jet moves following the trajectory marked by the nozzle. As the jet advances in the pool it slows down and the buoyancy force causes it to curve as the momentum in the axial direction is no longer predominant.

Air discharge through nozzles shows a characteristic evolution of pressures and velocities as it develops with respect to position.

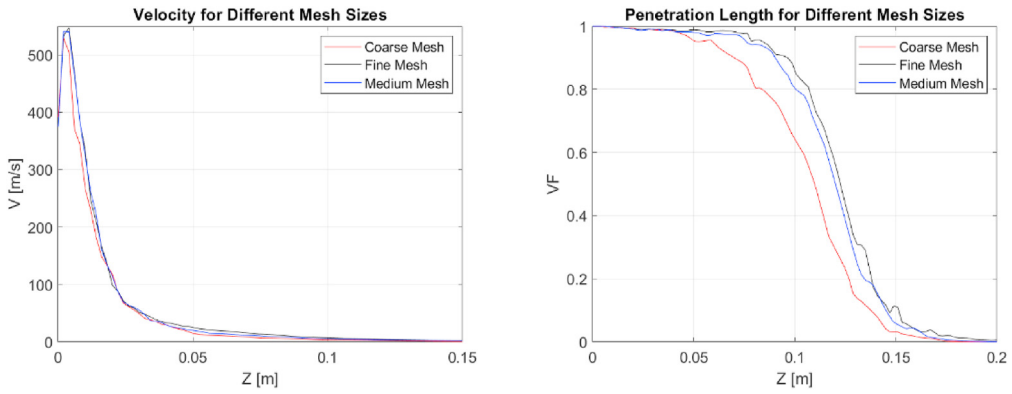

Fig. 2. Mesh independence test developed with nozzle of 4 mm and $\dot{m} = 0.0124\ kg/s$.

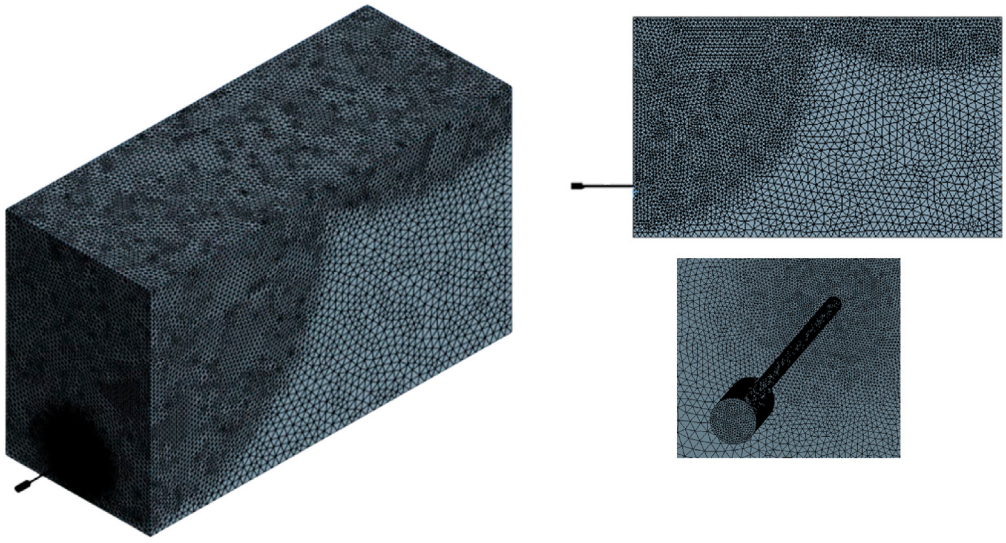

Fig. 3. Details of the spatial discretization of the geometric model.

Table 2
Summary of initial conditions of simulations.

	Test	$\dot{m}$ (*kg /h*)	u_0 (m/s)	ρ_0 (kg/m^3)	Fr_0	*Re* ($x\ 10^5$)	*Mach*
d_2	1	13.32	337	3.86	136.13	1.42	1.11
	2	10.44	272	3.66	117.42	1.09	0.96
	3	7.20	268	2.56	92.80	0.75	0.78
d_3	4	26.64	356	3.04	107.59	1.78	1.03
	5	20.16	313	2.63	90.66	1.35	0.95
	6	15.12	264	2.31	75.43	1.00	0.76
	7	12.24	248	1.99	65.30	0.81	0.71
d_4	8	44.64	351	2.88	90.52	2.21	1.01
	9	33.84	315	2.42	76.94	1.67	0.91
	10	20.88	243	1.93	56.31	1.03	0.70
	11	18.36	217	1.89	51.02	0.90	0.62
d_5	12	94.32	357	3.75	97.29	3.66	1.03
	13	64.08	297	3.09	78.40	2.51	0.85
	14	42.84	230	2.66	61.67	1.67	0.67
	15	31.32	213	2.11	49.79	1.22	0.62

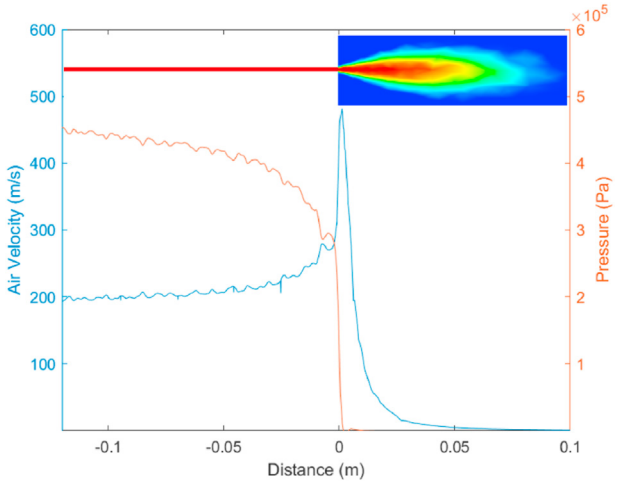

Fig. 4. Axial thermodynamic parameter inside the nozzle and at the nozzle outlet.

To reveal the flow behavior of the air flow at the nozzle and just after the nozzle exit when it expands, the axial distribution of both velocity and pressure has been plotted in Fig. 4. The air volume fraction is also plotted (in a top view, i.e., in a horizontal plane XZ at the nozzle height) to give an idea of the location and behavior of the air in this zone. As can be seen, the velocity increases along the nozzle until it reaches the maximum point and begins to decrease drastically until it becomes zero, i.e., the momentum force is no longer present, and the jet starts to bend in upward direction, and the buoyancy force becomes more important. The opposite occurs with the pressure which starts to decrease along the nozzle as it approaches the nozzle outlet and just after it goes drastically to zero.

The simulations carried out have a duration of 6 s, but the first 4 s are considered to reach stable conditions. To visualize the development of the jet, Fig. 5 shows the average air volume fraction during the last 2 s. At this point, the ANSYS simulation conditions are stabilized. The four tests of the 4 mm nozzle have been taken to exemplify the behavior. As can be seen the penetration length and width of the plume rise with the flow rate increase. In Fig. 5a, it can be seen that in addition to having the greatest plume width and the greatest jet penetration, there is greater water motion on the free surface caused by the higher flow rate. The opposite occurs in Fig. 5d, where the jet penetration is lower, the plume width is smaller and the water movement on the free surface is much smaller.

Another notable feature of these discharges is the pulsating condition of the jet. Fig. 6 shows four snapshots of the jet behavior for $Fr_0 = 91$ (test 8) spaced 50 ms from each other. The air jet is not continuous throughout its trajectory until it leaves the free surface. Instead, it breaks up as it moves towards the free surface, and the figure also shows that it occurs periodically, situation which makes advisable to perform a Fast Fourier Transform (FFT) to check if there is a dominant frequency in this phenomenon.

Fig. 7 shows the power spectral density (PSD) from the FFT analysis of plume width at a height of 0.25 m from the nozzle centerline. The processing was performed for all nozzle diameters and all flow rates to see the jet shape's periodicity, obtaining the dominant frequency in each simulation case. The breakup frequencies both in Fig. 6 and 7c ($Fr_0 = 91$s), occur approximately every 0.1 s, i.e., with a frequency of 10 Hz.

Almost all simulations exhibit similar trend with slight differences on their dominant frequency. In addition, in almost all cases,

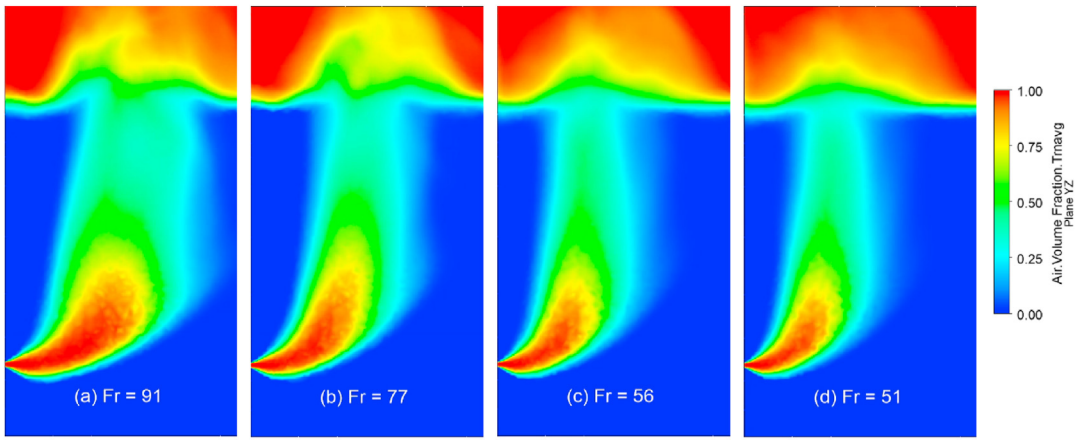

Fig. 5. Contour of Average Air Volume Fraction in 2 s for different mass flows rates.

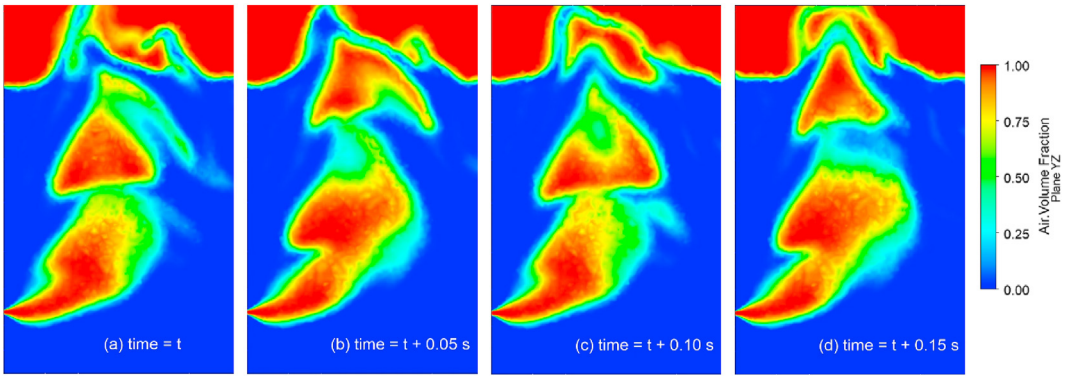

Fig. 6. Air volume fraction for $Fr_0 = 91$ at different times.

several harmonics of smaller magnitude appear approximately every 10 Hz of the dominant frequency. For the smallest nozzle diameters (Fig. 7a), the value of the frequency magnitude is much smaller than in the other nozzle diameters, so probably the dominant frequency is less important than in the other simulations. In other words, the jet remains more of a continuum until the air exits the free surface. In addition, there is a slight trend showing how the dominant frequencies become smaller with higher Froude number values. This pattern is respected in all cases except for the test with the highest Froude number for the 2 mm nozzle. On the other hand, it is also observed that the frequency decreases for larger nozzle sizes.

5.2. Jet penetration length

One of the objectives of this work is to study the behavior of the jet penetration length and its dependence on the initial conditions of the discharge, both geometric and flow/pressure. A way to observe more clearly the behavior of the jet penetration length is by obtaining the axial distribution of air volume fraction along the centerline of the nozzle. Table 3 shows the average values, maximum, minimum and deviation of the moment length for each of the simulations developed over the time in which the statistical analysis was performed. To estimate the penetration length, the area under the curve of volume fractions versus distance was calculated (Table 3) using trapezoidal numerical integration. The resulting value for the penetration length (L_m) was obtained for each of the cases analyzed.

As can be seen in Table 3, for all nozzle diameters the largest momentum length corresponds to the largest discharged air flow rate. Table 3 also includes a column with the standard deviation of the penetration length over the 2-s statistics. This variable allows to get a better understanding on the instantaneous variation of the jet penetration. The standard deviation of the momentum length increases for higher nozzle diameters although the largest one is 3.7 mm for the case of diameter 4 and higher flowrate. Generally, the momentum length variation increases with the nozzle diameter but only in absolute values (this does not happen if we use relative values). All instantaneous values fall 95% of the time within a range of no more than ±6.4%, except for test 12, where this range rises to ±9.5%.

A comparison between the CFD predictions and the experimental results obtained by Harby et al. [8] was carried out. Fig. 8 shows the comparison (simulation and experimental) of the gas jet penetration length for different mass flow rates and nozzle diameters, where the subscripts E and S are the results of the experiment and simulation respectively for each of the diameters. Both in the simulation and the experiment, it is observed that the penetration length increases with the flow rate. On the other hand, with a similar flow rate, longer lengths are obtained with smaller diameter nozzles. As a general trend, the simulations performed with ANSYS CFX slightly underestimate the momentum length measured in the experimental reference case [8]. The trend lines for each of the nozzle diameters are also presented and are observed to be increasing. Except for some case with the smaller nozzles, the tests are within the error bands of the experimental measurements.

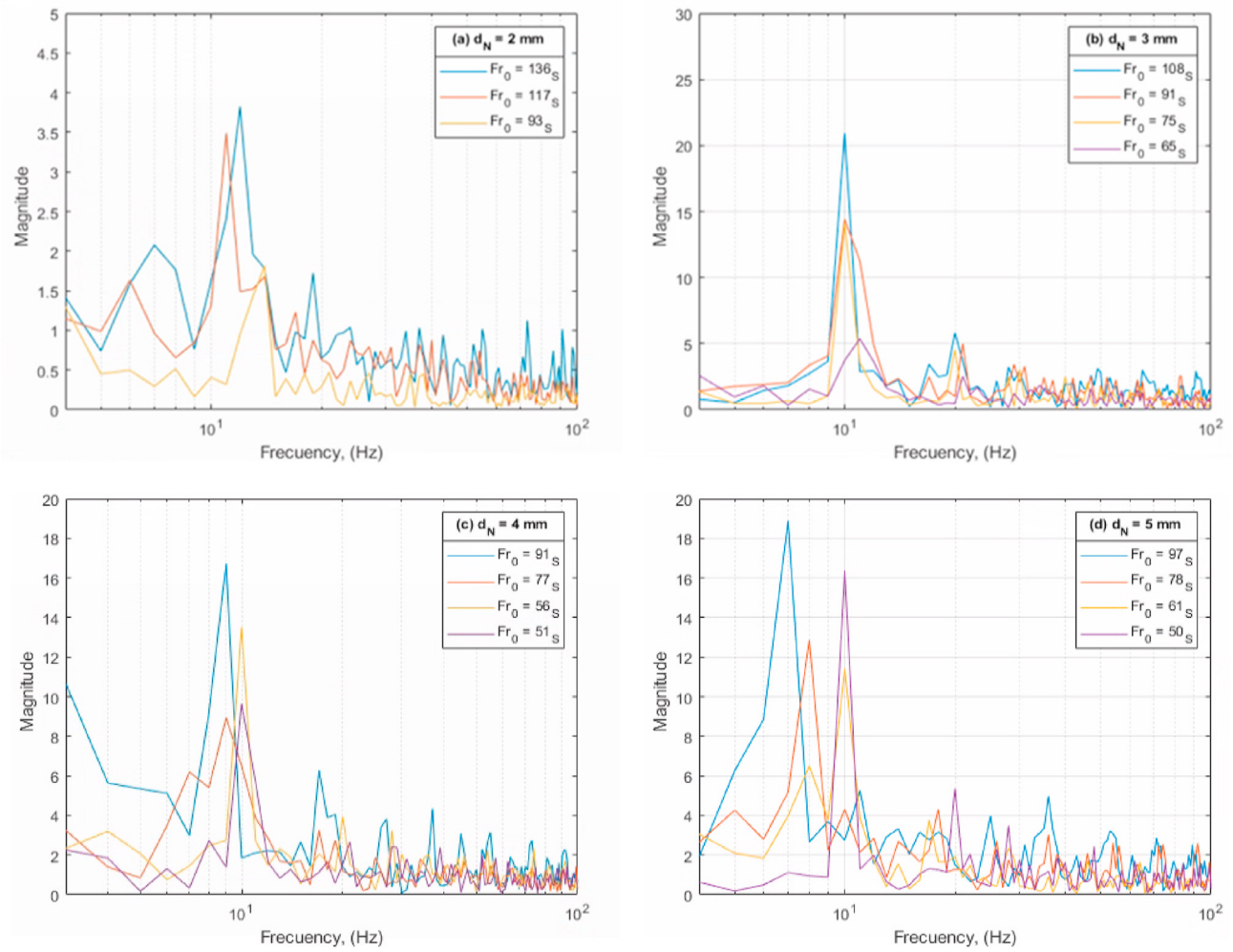

Fig. 7. *Frequency spectrum of plume width at a height of 0.25 m from the nozzle, a)* d_N = 2 mm, *b)* d_N = 3 mm, *c)* d_N = 4 mm, *d)* d_N = 5 mm.

Table 3
Average values of momentum length obtained in the simulations.

	Test	$\overline{L_m}$ *(mm)*	*Max (mm)*	*Min (mm)*	*σ (mm)*
d_2	1	64.6	66.4	62.4	1.2
	2	58.7	60.4	56.4	0.8
	3	49.3	48.9	49.6	0.2
d_3	4	89.4	92.6	86.6	1.5
	5	77.5	78.5	76.5	1.0
	6	68.6	70.5	68.5	0.5
	7	58.5	60.4	56.4	1.1
d_4	8	116.2	122.8	110.7	3.7
	9	94.2	98.7	92.6	1.6
	10	79.3	84.6	76.5	2.5
	11	69.8	74.5	66.4	2.1
d_5	12	146.7	173.2	136.9	7.0
	13	129.4	138.9	122.8	3.5
	14	103.2	108.7	100.7	2.2
	15	87.6	90.6	84.6	1.8

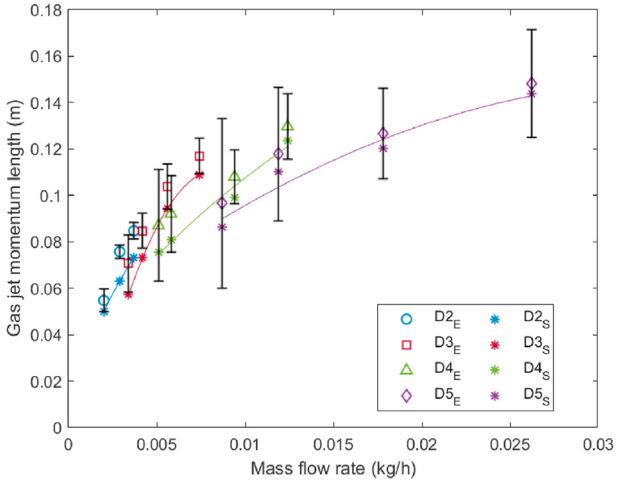

Fig. 8. Comparison of penetration length at different mass flow rates between CFD and experimental results.

5.3. Jet buoyancy length

The buoyancy length was also obtained from the evolution of the void fraction. In this case, a line has been placed at a height of 0.25 m above the nozzle. This height is chosen because it is considered that the jet is sufficiently developed so that only buoyancy forces act and the trajectory is essentially vertical. In addition, it is sufficiently below the free surface so that no distortions appear. On this line, starting from the end opposite the nozzle,

the point at which the air appears is obtained to determine the position of the interface. The total horizontal length of the jet will be delimited between the nozzle and this point. The value of L_m must be subtracted from the total length calculated to obtain L_b.

Table 4 shows the average values, maximum, minimum and standard deviation of the buoyancy length for each of the simulations developed over the time in which the statistical analysis was performed. As shown in the table, there is a significant oscillation of the buoyancy length during the analyzed period. Unlike the momentum length, the buoyancy range is much more susceptible to variation due to the accumulation of air in bubbles during ascent. Therefore, by analyzing the instantaneous behavior of this variable, it is possible to identify the appearance of air clusters that move intermittently following the reasoning observed in Fig. 6. For the 2 and 3 mm nozzles, the instantaneous values are 95% of the time within a range between 20% and 30%, but for the larger nozzles this value is even exceeded. The variation of the buoyancy length becomes more evident as the nozzle diameter increases, and the maximum value of the standard deviation is observed in the largest diameter (5 mm), which represents a value slightly below 40% of the mean value. A particular case is observed in Test 8 where the minimum instantaneous value of the buoyancy length is close to zero. In this case a particularly isolated air cluster is observed, leading to a very low value for that specific moment. Nevertheless, the standard deviation shows that it is not a trend but an outlier.

The buoyancy length indicates the maximum distance reached horizontally from the nozzle. This length is bounded from the point at which the momentum length is delimited to the distance at which the envelope shows a vertical projection. Fig. 9 shows the comparison of the behavior of buoyancy length as a function of mass flow rate for both the simulation results and the experimental results reported by Harby et al. [8]. The subscripts E and S are the results of the experiment and simulation respectively for each of the diameters. The trend lines for each of the nozzle diameters are also presented and are observed to be increasing, which is because, as the air mass flow increases, the expansion that exists will increase the distance at which this jet will penetrate and, in turn, the buoyancy distance will be greater. There is a noteworthy overestimation in the length obtained for the tests of the larger nozzles with higher air flow. Given the clear trend obtained in the simulations performed and the irregularity presented in the results of this variable in the reference experiments [8], it can be assessed the possibility that there were some limitations in the process of obtaining the buoyancy length in the mentioned experiment.

Table 4
Average values of buoyancy length obtained in the simulations.

	Test	$\overline{L_b}$ *(mm)*	*Max (mm)*	*Min (mm)*	*σ (mm)*
d_2	1	85.6	106.7	60.4	13.8
	2	74.3	84.6	52.3	10.7
	3	59.4	66.4	56.4	1.8
d_3	4	128.8	157.0	86.6	21.4
	5	111.4	136.9	74.5	19.6
	6	85.7	108.7	48.3	14.0
	7	74.5	90.6	44.3	8.4
d_4	8	164.6	232.2	0.7	46.0
	9	136.0	175.5	72.1	25.6
	10	90.1	161.1	28.2	18.4
	11	69.9	114.8	30.2	21.5
d_5	12	208.5	370.5	66.4	80.0
	13	161.1	256.7	29.2	55.1
	14	141.7	192.6	73.2	34.6
	15	115.6	147.0	68.5	25.2

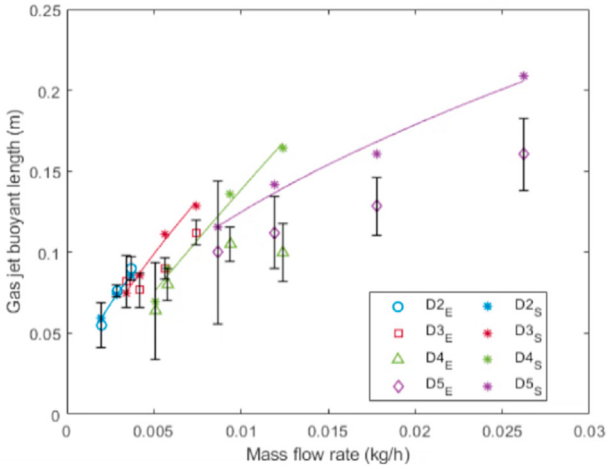

Fig. 9. Comparison of buoyancy length at different mass flow rates between CFD and experimental results.

5.4. Correlations for the penetration and buoyancy lengths

From the results of the simulations performed a best-fit correlation is obtained using dimensionless numbers such as Froude, Reynolds and Mach numbers. After analyzing the performance in predicting penetration length of the different dimensionless number involved in the phenomenon, a correlation that depends on both Fr_0 and *Mach* is proposed. In order to analyze this dependence, the penetration length has been normalized with a characteristic length (L_Q), defined as the square root of the nominal nozzle area ($\sqrt{A_N}$). Fig. 10 illustrates the normalized jet penetration length obtained from Equation (9) (L_m/L_Q predicted) versus the one obtained in the simulations (L_m/L_Q *simulated*) for each of the nozzle diameters.

The data follow a quasi-power relationship and can be represented by Equation (9), with a coefficient of determination of $R^2 = 0.915$. As can be seen from the exponents to which Fr_0 and *Mach* are raised in Equation (9), the momentum length have a direct dependence with both dimensionless numbers, with the Mach number having the greatest influence.

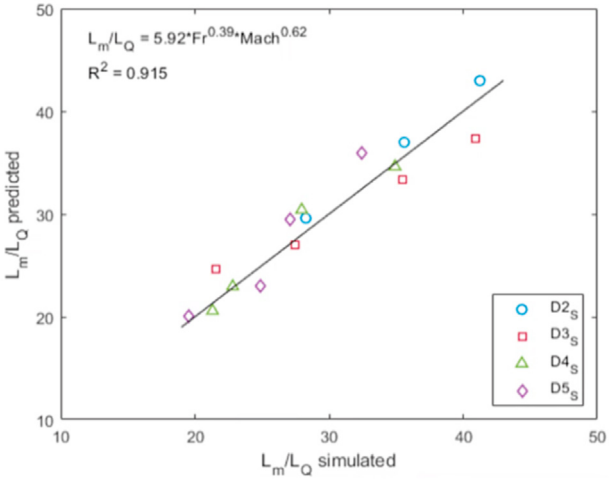

Fig. 10. Normalized momentum lengths (simulated) in function of normalized momentum lengths (predicted) with Equation (9).

$$\frac{L_m}{L_Q} = 5.92 * {Fr_0}^{0.39} Mach^{0.62} \quad (9)$$

The same procedure has been followed to correlate the buoyancy length with dimensionless numbers. In this case a better correlation of the data with Froude and Reynolds numbers was obtained. Fig. 11 shows the normalized buoyancy length (L_b/L_Q predicted), obtained from Equation (10), versus the one obtained in the simulations (L_b/L_Q *simulated*) for each of the nozzle diameters.

As well as with the normalized buoyancy length the data follow a quasi-power relationship, with a coefficient of determination of $R^2 = 0.922$. The dimensionless length of the momentum has a direct dependence on the dimensionless numbers Fr_0 and *Re*.In this case, the Froude number has a greater influence.

$$L_b \Big/ L_Q = 0.12 * {Fr_0}^{0.68} Re^{0.23} \quad (10)$$

As can be seen in both Figs. 10 and 11, both lengths are related to the Froude number. Both correlations obtained have an R^2 greater than 0.9, so it can be determined that there is a good linear relationship. On the other hand, the dimensionless numbers used indicate that these lengths have a strong dependence on inertial forces.

6. CFD model validation

Another purpose of this study is to validate the developed model with the experimental results presented by Harby et al. [8,9]. The simulation starts at time 0 s, so that the first 4 s of simulation are necessary for the discharge to be stabilized. All calculated parameters are the result of a statistical analysis of the following 2 s of simulation.

6.1. Normalized penetration length validation

To validate the developed computational model, the CFD results of gas jet momentum length for different mass flow rates and nozzle diameters were compared with the experimental results. Furthermore, this validation would corroborate that this model allows to simulate the behavior of non-condensable gas jets discharged in subcooled water. Fig. 12 shows the comparison of the dimensionless penetration length obtained in the simulation versus those obtained in the reference experiments [8].

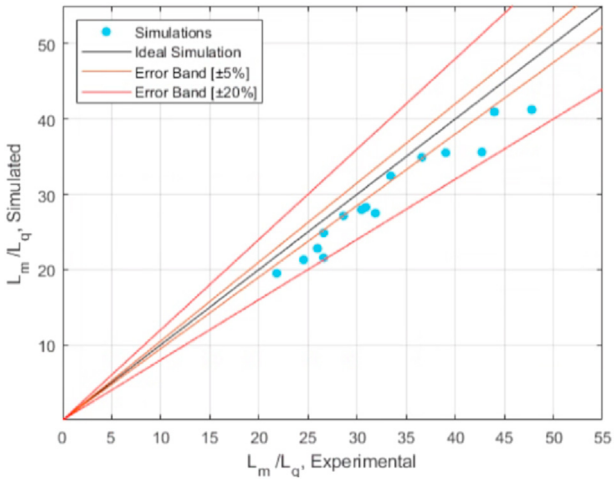

Fig. 12. Comparison of normalized penetration length (predicted) and normalized penetration length (simulated).

The simulations show satisfactory results in terms of obtaining the momentum length. Many of the values are within the 5% error band and the maximum error obtained between both results is 18%, which is considered acceptable results that allow using this model and simulating different flow rates and diameters. As can be seen, the results of the simulation underpredicted the experiments results for the dimensionless penetration length. It should be considered that this aspect may be due to multiple factors. The values may have been slightly shifted by aspects related to the numerical diffusion of the simulation or due to a systematic error of the experimental process, having created an increase in the length of the results. It should be taken into account that results are being compared between two methodologies, where the proper process of obtaining measurements for experiments is different from that of simulations.

6.2. Normalized buoyancy length validation

Fig. 13 shows the comparison of the normalized buoyancy length obtained in the simulations versus the normalized buoyancy

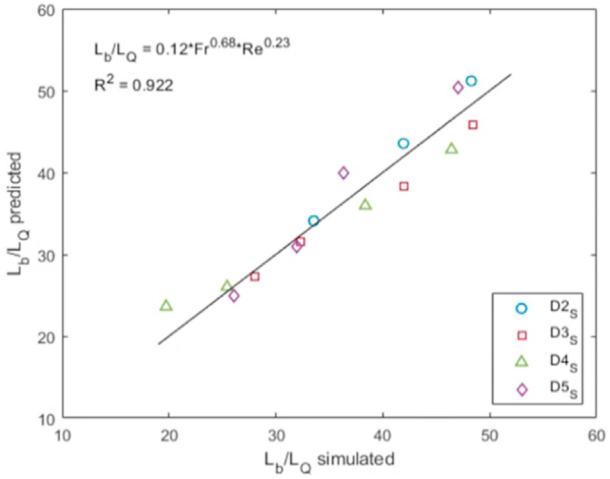

Fig. 11. Normalized buoyancy lengths (simulated) in function of normalized buoyancy lengths (predicted) with Equation (10).

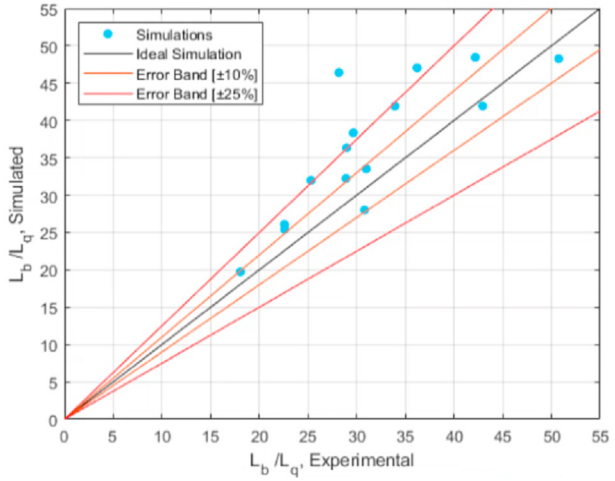

Fig. 13. Comparison of normalized buoyancy length (predicted) and normalized buoyancy length (simulated).

length obtained by Harby et al. [8]. As can be seen, there is more dispersion of the simulation results with respect to the experimental results for the dimensionless buoyancy length. In this case, it is logical that a greater dispersion appears because this length depends on the maximum distance reached by the jet and the momentum length. These two quantities are variable throughout a simulation (in the case of the momentum length there is dependence on the position of the interface along the horizontal projection of the jet and on the position of the nozzle itself, but the latter is a fixed position). Also, as for the momentum length, there is a tendency between experimental measurements and simulates, but in this case to overestimate rather than underestimate the results. The higher flow rate tests for larger nozzles tend to show more of this phenomenon, which may indicate some systematic error in capturing the measurements. As is the case for moment length, there may be several causes for this overestimation, attributable both to the code and/or to experimentation.

6.3. Jet centerline validation

Fig. 14 shows a comparison of the results obtained from experimentally measured jet trajectories by Harby et al. [9], those calculated theoretically with a model also proposed in that paper and the results obtained from simulations performed in the current study with the ANSYS CFX code. The Froude number has a significant influence on the trajectory of the jet, as can be seen in Fig. 14. Increasing the Froude number increases the horizontal distance at which the jet is located.

Overall, in the 3 cases (experiment, theoretical model and CFD simulations) the trajectories are quite similar. Harby's model and the correlations obtained with the ANSYS CFX code show very similar trajectories, even large overlaps can be appreciated. It is worth noting the similarity in the cases of the 2 and 5 mm nozzles (Fig. 14a and d). The curves of the simulations follow a trajectory faithful to that of the Harby's model over the entire horizontal distance range. For the cases of the 3 and 4 mm nozzles (Fig. 14b and c) some accuracy is lost at positions closer to the nozzle. It is also noticeable that the CFD model tends to underestimate the results for low Froude number in some cases, such as for the 4 mm nozzle inner diameter (Fig. 14c). Another noteworthy finding is the good trajectory capture in the simulations for larger vertical distances. The horizontal distances are very similar between the simulations, the theoretical model and the experimental measurements when the jet trajectory reaches some height. In contrast, it can be seen that the largest mismatches occur generally at low altitudes, and it can be interpreted that the simulations tend to curve the jet in an area closer to the nozzle.

7. Conclusions

This paper shows the results obtained from a 3D model developed using CFD codes, specifically ANSYS CFX software, of air discharges in a pool with subcooled water. Different nozzle diameters and air mass flows were analyzed. The results obtained were validated with those experimental reported by Harby et al. [8,9], obtaining a good agreement between both. The investigations presented in this paper focus on the jet behavior characterized by penetration length and buoyancy length. The main conclusions

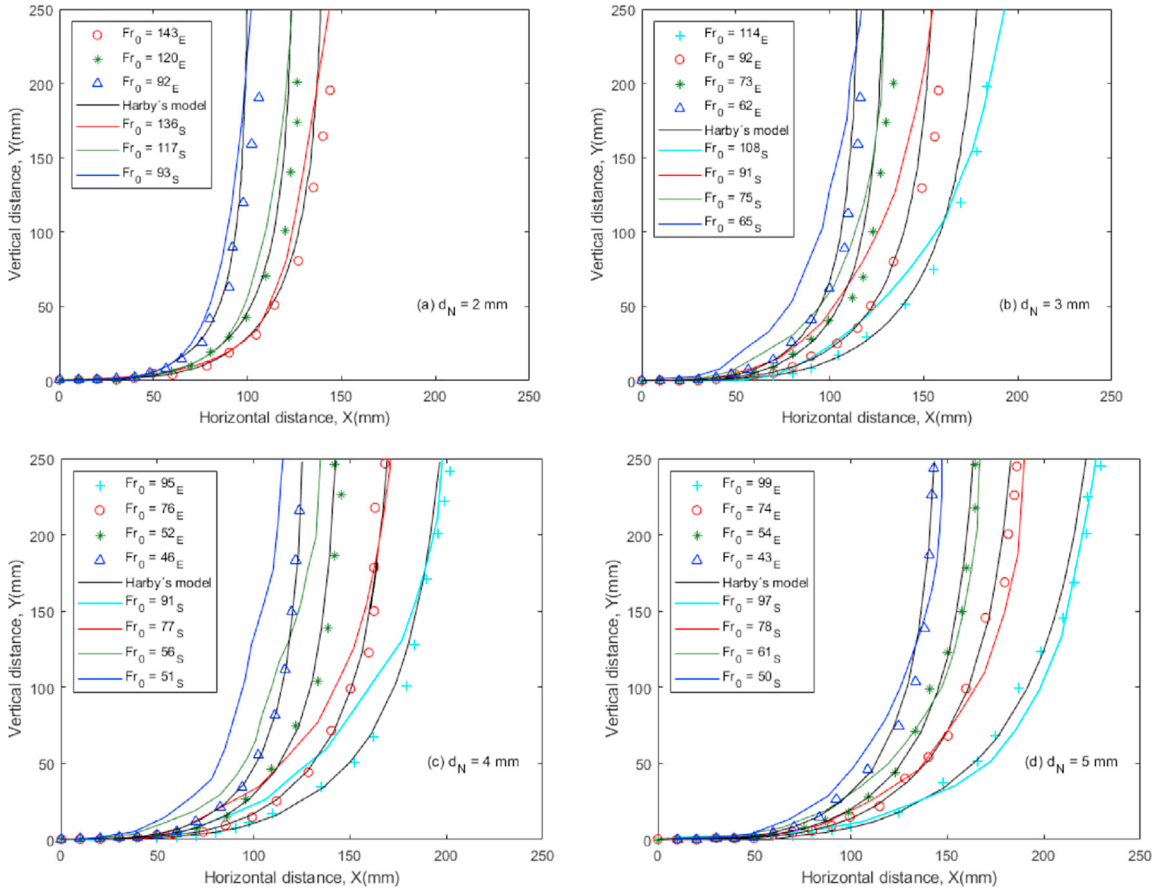

Fig. 14. Comparison of centerline jet trajectories for experimental, theorical and numerical.

obtained are as follows:

(1) The air reaches a greater penetration length as its flow rate increases while also increasing the cross section over which it extends. So that each flow rate as it move away from the centerline decreases the fraction of air until it becomes zero, while also increasing the area occupied by this in its cross-section (more or less circular) as we move away from the nozzle.
(2) A correlation of dimensionless penetration length as a function of Froude number and Mach number was obtained and this dependence follows a power distribution with a coefficient of determination of $R^2 = 0.915$, which means that it fits very well.
(3) A correlation of dimensionless buoyancy length as a function of Froude number and Reynolds number was obtained and this dependence follows a power distribution with a coefficient of determination of $R^2 = 0.922$.
(4) An FFT analysis of the plume width at a height of 0.25 m from the nozzle was performed, where it was obtained that the breakup frequency occurs for most of the simulations at or around 10 Hz. For the smaller diameters cases this dominant frequency was less important than in the rest of the simulations.
(5) The results obtained in these simulations were validated with those reported in the experiments performed by Harby et al. [9],it was observed that the CFD results underestimated the experimental results for the dimensionless momentum length but most of the results were found to be within the band of 5%. While for the buoyancy length, the results from the CFD deviated more from the experimental results, with half of them falling within a 10% band of error.
(6) The jet trajectory has a strong dependence on inertial forces. Increasing the Froude number increases the horizontal distance at which the jet is located, which is in agreement with both the experimental and theoretical results previously obtained by Harby et al. [9].
(7) Based on the results of the simulation, it can be concluded that the CFD numerical model used in this work can be used to simulate the behavior of non-condensable gases discharged in water.

Declaration of competing interest

The authors declare that they have no known competing financial interests or personal relationships that could have appeared to influence the work reported in this paper.

Acknowledgments

This work was supported by the project THAIS co-financed by the CSN (Nuclear Safety Council of Spain) and the UPV (Polytechnical University of Valencia). The authors also would like to express gratitude to the Generalitat Valenciana (Spain) for its support under the Santiago Grisolía Program/2018/140.

References

[1] J.L. Muñoz-Cobo, D. Blanco, C. Berna, Y. Córdova, Review of instabilities produced by direct contact condensation of steam injected in water pools and tanks, Prog. Nucl. Energy 153 (2022), https://doi.org/10.1016/j.pnucene.2022.104404.
[2] Y. Córdova, D. Blanco, C. Berna, J.L. Muñoz-Cobo, A. Escrivá, Y. Rivera, Experimental characterization of the dimensionless momentum length for submerged jet discharges of air-steam mixtures into stagnant water, Int. J. Comput. Methods Exp. Meas. 10 (2022) 195–210, https://doi.org/10.2495/cmem-v10-n3-195-210.
[3] B. Pershagen, LIGHT WATER REACTOR SAFETY Probabilistic Risk Assessment in the Nuclear Power Industry, 1989.
[4] X. Wang, D. Grishchenko, P. Kudinov, Pre-test analysis for definition of steam injection tests through multi-hole sparger in PANDA facility, Nucl. Eng. Des. 386 (2022), 111573, https://doi.org/10.1016/j.nucengdes.2021.111573.
[5] Y. Zhang, D. Lu, Z. Wang, X. Fu, Q. Cao, Y. Yang, G. Wu, Experimental research on the thermal stratification criteria and heat transfer model for the multi-holes steam ejection in IRWST of AP1000 plant, Appl. Therm. Eng. 107 (2016) 1046–1056, https://doi.org/10.1016/j.applthermaleng.2016.07.083.
[6] Y.-T. Moon, H.-D. Lee, G.-C. Park, CFD simulation of steam jet-induced thermal mixing in subcooled water pool, Nucl. Eng. Des. 239 (2009) 2849–2863, https://doi.org/10.1016/j.nucengdes.2009.08.003.
[7] J. Wang, L. Chen, Q. Cai, C. Hu, C. Wang, Direct contact condensation of steam jet in subcooled water: a review, Nucl. Eng. Des. 377 (2021) 1–28, https://doi.org/10.1016/j.nucengdes.2021.111142.
[8] K. Harby, S. Chiva, J.L. Muñoz-Cobo, An experimental investigation on the characteristics of submerged horizontal gas jets in liquid ambient, Exp. Therm. Fluid Sci. 53 (2014) 26–39, https://doi.org/10.1016/J.EXPTHERMFLUSCI.2013.10.009.
[9] K. Harby, S. Chiva, J.L. Muñoz-Cobo, Modelling and experimental investigation of horizontal buoyant gas jets injected into stagnant uniform ambient liquid, Int. J. Multiphas. Flow 93 (2017) 33–47, https://doi.org/10.1016/j.ijmultiphaseflow.2017.03.008.
[10] M.R. Davidson, Flow in the stagnation zone during sumerged injection of a swirling gas jet, Chem. Eng. Sci. 45 (1990) 687–694.
[11] G.H. Jirka, Integral model for turbulent buoyant jets in unbounded stratified flows. Part I: single round jet, Environ. Fluid Mech. 4 (2004) 1–56, https://doi.org/10.1023/A:1025583110842.
[12] A.H. Castillejos, J.K. Brimacombe, Measurement of physical characteristics of bubbles in gas-liquid plumes: Part I. An improved electroresistivity probe technique, Metall. Trans. B 18 (1987) 649–658, https://doi.org/10.1007/BF02672881.
[13] K. Ito, S. Kobayashi, M. Tokuda, Measured Using an Isokinetic Sampling Probe II o ssu 22 (1991) 439–445.
[14] W. Li, Z. Meng, Z. Sun, L. Sun, C. Wang, Investigations on the penetration length of steam-air mixture jets injected horizontally and vertically in quiescent water, Int. J. Heat Mass Tran. 122 (2018) 89–98, https://doi.org/10.1016/j.ijheatmasstransfer.2018.01.075.
[15] Y. Córdova, Y. Rivera, D. Blanco, C. Berna, J.L. Muñoz-Cobo, A. Escrivá, Experimental investigation of submerged horizontal air–steam mixture jets into stagnant water, Adv. Fluid Mech. XIII. 1 (2020) 89–101, https://doi.org/10.2495/afm200091.
[16] W. Li, Z. Meng, J. Sun, W. Cai, Y. Hou, Air horizontal jets into quiescent water, Nucl. Eng. Technol. (2023) 15, https://doi.org/10.1016/j.net.2023.02.024.
[17] B.U.N. Igwe, S. Ramachandran, J.C. Fulton, Jet penetration and liquid splash in submerged gas injection, Metall. Trans. A 4 (1973) 1887–1894, https://doi.org/10.1007/BF02665417.
[18] E.O. Hoefele, J.K. Brimacombe, Flow regimes in submerged gas injection, Metall. Trans. B 10 (1979) 631–648, https://doi.org/10.1007/BF02662566.
[19] J.L. Carreau, F. Roger, L. Loukarfi, L. Gbahoue, P. Hobbes, Penetration of a horizontal gas jet sumerged in a liquid, in: Proc. Intersoc. Energy Convers. Eng. Conf., 1986, pp. 315–319.
[20] A. Emani, C. Briens, Study of downward gas jets into a liquid, AlChe J 54 (2008) 2269–2280, https://doi.org/10.1002/aic.
[21] H.Y. Kim, Y.Y. Bae, C.H. Song, J.K. Park, S.M. Choi, Experimental study on stable steam condensation in a quenching tank, Int. J. Energy Res. 25 (2001) 239–252, https://doi.org/10.1002/er.675.
[22] X.-Z. Wu, J.-J. Yan, W.-J. Li, D.-D. Pan, D.-T. Chong, Experimental study on sonic steam jet condensation in quiescent subcooled water, Chem. Eng. Sci. 64 (2009) 5002–5012, https://doi.org/10.1016/j.ces.2009.08.007.
[23] J. Yan, X. Wu, D. Chong, Experimental study on pressure and temperature distributions for low mass flux steam jet in subcooled water, Sci. China, Ser. E Technol. Sci. 52 (2009) 1493–1501, https://doi.org/10.1007/s11431-009-0177-2.
[24] Z. Meng, W. Zhang, J. Liu, R. Yan, G. Shen, Experimental study on the condensation of sonic steam in the underwater environment, Nucl. Eng. Technol. 51 (2019) 987–995, https://doi.org/10.1016/j.net.2019.02.003.
[25] D. Zhang, L. Tong, X. Cao, Condensation oscillation characteristic of steam with non-condensable gas through multi-hole sparger at low mass flux, Nucl. Eng. Technol. 55 (2022) 780–791, https://doi.org/10.1016/j.net.2022.10.001.
[26] J.M.-C. Lin, Transient Gas Jets into Liquid, 1986.
[27] T.A. Engh, M. Nilmani, Bubbling at high flow rates in inviscid and viscous liquids (slags), Metall. Trans. B 19 (1988) 83–94, https://doi.org/10.1007/BF02666494.
[28] Z. Dai, B. Wang, L. Qi, H. Shi, Experimental study on hydrodynamic behaviors of high-speed gas jets in still water, Acta Mech. Sin. Xuebao. 22 (2006) 443–448, https://doi.org/10.1007/s10409-006-0029-2.
[29] H.H. Shi, B.Y. Wang, Z.Q. Dai, Research on the mechanics of underwater supersonic gas jets, Sci. China Phys. Mech. Astron. 53 (2010) 527–535, https://doi.org/10.1007/s11433-010-0150-x.
[30] A. Mersmann, Flooding point of liquid/liquid countercurrent columns, Chem. Eng. Technol. 52 (1980).
[31] ANSYS Inc, Ansys CFX-Solver Theory Guide, Version-2022R1, 2022, p. 386.
[32] ANSYS Inc, Ansys CFX-Solver Modeling Guide, Version-2022R1, 2022, p. 740.
[33] S.S. Gulawani, J.B. Joshi, M.S. Shah, C.S. RamaPrasad, D.S. Shukla, CFD analysis

of flow pattern and heat transfer in direct contact steam condensation, Chem. Eng. Sci. 61 (2006) 5204–5220, https://doi.org/10.1016/j.ces.2006.03.032.
[34] A. Shah, I.R. Chughtai, M.H. Inayat, Numerical simulation of direct-contact condensation from a supersonic steam jet in subcooled water, Chin. J. Chem. Eng. 18 (2010) 577–587, https://doi.org/10.1016/S1004-9541(10)60261-3.
[35] V. Tanskanen, A. Jordan, M. Puustinen, R. Kyrki-Rajamäki, CFD simulation and pattern recognition analysis of the chugging condensation regime, Ann. Nucl. Energy 66 (2014) 133–143, https://doi.org/10.1016/j.anucene.2013.12.007.
[36] X.-H. Qu, H. Sui, M.-C. Tian, CFD simulation of steam-air jet condensation, Nucl. Eng. Des. 297 (2016) 44–53, https://doi.org/10.1016/j.nucengdes.2015.11.011.
[37] L. Zhou, D. Chong, J. Liu, J. Yan, Numerical study on flow pattern of sonic steam jet condensed into subcooled water, Ann. Nucl. Energy 99 (2017) 206–215, https://doi.org/10.1016/j.anucene.2016.08.024.
[38] L. Wang, X. Yue, Q. Zhao, D. Chong, J. Yan, Numerical investigation on the effects of steam and water parameters on steam jet condensation through a double-hole nozzle, Int. J. Heat Mass Tran. 126 (2018) 831–842, https://doi.org/10.1016/j.ijheatmasstransfer.2018.05.090.
[39] A. Graževičius, A. Bousbia-Salah, Comparative study of CFD and 3D thermal-hydraulic system codes in predicting natural convection and thermal stratification phenomena in an experimental facility, Nucl. Eng. Technol. (2023) 19, https://doi.org/10.1016/j.net.2023.02.017.
[40] S.Q. Li, P. Wang, T. Lu, Numerical simulation of direct contact condensation of subsonic steam injected in a water pool using VOF method and LES turbulence model, Prog. Nucl. Energy 78 (2015) 201–215, https://doi.org/10.1016/j.pnucene.2014.10.002.
[41] S.K. Dahikar, M.J. Sathe, J.B. Joshi, Investigation of flow and temperature patterns in direct contact condensation using PIV, PLIF and CFD, Chem. Eng. Sci. 65 (2010) 4606–4620, https://doi.org/10.1016/j.ces.2010.05.004.
[42] M. Germano, U. Piomelli, P. Moin, W.H. Cabot, A dynamic subgrid-scale eddy viscosity model, Phys. Fluids A. 3 (1991) 1760–1765, https://doi.org/10.1063/1.857955.
[43] D.K. Lilly, A proposed modification of the Germano subgrid-scale closure method, Phys. Fluids 4 (1992) 633–635, https://doi.org/10.1063/1.858280.
[44] NEA/CSNI, Best Practice Guidelines for the Use of CFD in Nuclear Reactor Safety Applications - Revision, 2015.
[45] ANSYS Inc, ANSYS 2022 R1 - Meshing User's Guide, 2022.